Granular Matter (2013) 15:209–220
DOI 10.1007/s10035-013-0399-7

ORIGINAL PAPER

A simple distinct element modeling of the mechanical behavior of methane hydrate-bearing sediments in deep seabed

M. J. Jiang · Y. G. Sun · Q. J. Yang

Received: 3 May 2012 / Accepted: 5 February 2013 / Published online: 24 February 2013

Abstract The study on the mechanical behavior of methane hydrate-bearing sediments (HBS) in deep seabed is of great significance for the safe exploitation of methane hydrate in the future. Recent studies have shown that the mechanical behavior of HBS is significantly influenced by methane hydrate since it leads to cementation among soil grains. For better understanding its microscopic mechanical mechanism, this paper presents a simple numerical model of HBS using the distinct element method (DEM). First, a set of tests on two bonded aluminum rods were performed under different loading paths with a specially designed apparatus. Then, a simple bond contact model was proposed based on the experimental data and implemented into our two-dimensional DEM code, NS2D. Finally, a series of drained biaxial compression tests under different confining stresses on HBS samples with different bond strengths, which are used to represent different methane hydrate saturations (S_{MH}), were carried out with this code. By comparing the results of numerical simulations with the experimental data obtained from triaxial compression tests, the study shows that the DEM incorporating the new bond contact model is capable of capturing the main mechanical characteristics of HBS such as the strain softening and dilation. And it can also capture that (a) the peak shear strength increases as S_{MH} or the confining stress increases, while the dilation increases as S_{MH} increases or the confining stress decreases; (b) both the cohesion and friction angle increase with the increasing of S_{MH}, but the influence of S_{MH} on the cohesion is much more significant than on the friction angle.

Keywords Methane hydrate-bearing sediments · Mechanical properties · Cementation · Contact behaviour · Distinct element method

M. J. Jiang (✉)· Y. G. Sun · Q. J. Yang
Department of Geotechnical Engineering,
College of Civil Engineering, Tongji University,
1239 Siping Road, Shanghai 200092, China
e-mail: mingjing.jiang@mail.tongji.edu.cn;
mingjing.jiang@tongji.edu.cn

M. J. Jiang · Y. G. Sun · Q. J. Yang
Key Laboratory of Geotechnical and Underground Engineering
of Ministry of Education, Tongji University, Shanghai, China

1 Introduction

Methane hydrate-bearing sediments (HBS) are a kind of natural soil deposits that contain methane hydrate, which is a class of solid materials in which methane molecules occupy "cages" made up of hydrogen-bonded water molecules, in their pores. The methane hydrate (MH) is formed under the high pressure and low temperature. In natural environment, this material can only develop and exist in deep seabed or permafrost regions. Because of the large amount of methane hydrate accumulating in the earth crust, of which the carbon content is twice as much as that of fossil fuel, the MH is considered to be extremely meaningful to alleviate the aggravating energy crisis. Therefore, to date, some countries have drawn up their national research programs to investigate the technologies for exploiting methane hydrate from HBS, such as Japan, United states, India, China and South Korea [36].

It has been acknowledged that MH plays an important role on the mechanical properties of HBS, e.g. its strength increases with the increasing of the hydrate saturation (S_{MH}). Hence, the dissociation of methane hydrate in HBS due to the exploitation will reduce its strength, which may lead to some geotechnical and geoenvironmental engineering problems or disasters. Some endeavors have been devoted to investigate submarine geohazard, such as the initiation of marine landsides due to hydrate dissociation [1,34,43], and

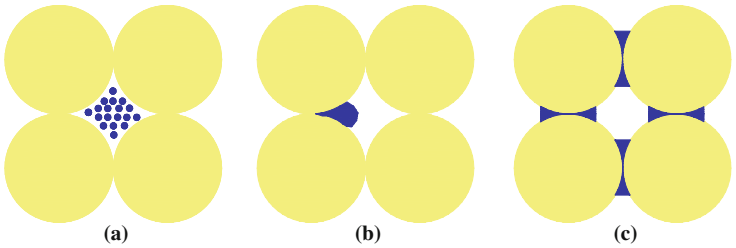

Fig. 1 Pore-scale distribution of methane hydrate: **a** Pore-filling; **b** load-bearing; **c** cementation. The *graph* is redrawn from Waite et al. [54]

wellbore instability in methane hydrate bearing sediments during methane gas production [8,35,46,47]. It is well known that the applicability of all these researches largely depends on the accuracy of the employed constitutive relations which are used to describe the mechanical behavior of HBS, on one hand. Unfortunately, on the other hand, the mechanical properties of this material are not completely known yet for many reasons, for example, the technical difficulty in field sampling and the limited knowledge on the formation mechanism of methane hydrate in HBS.

The previous researches have revealed that the properties of HBS are affected not only by S_{MH} [41,42], but also by the hydrate distribution governed by the hydrate nucleation and growing process [9,40]. As shown in Fig. 1, Waite et al. [54] have described the hydrate distribution in sediments with three models, i.e. pore-filling as fine particles in Fig. 1a, loading-bearing in combination with skeleton coarse particles in Fig. 1b, and cementation at contacts between particles in Fig. 1c. Previous investigations show that these differences on the distribution of methane hydrate comes from differences on environments that lead to methane hydrate, and will affect the mechanical behavior of HBS in different ways. In order to understand how the hydrate distribution influences the intermediate and large strain behavior and the failure condition, Brugada et al. [2] have investigated the geomechanical behavior of HBS which had a pore-filling hydrate distribution with a distinct element method (DEM) code, PFC^{3D}. The result shows that the contribution of this hydrate distribution to the strength of HBS was of a frictional nature rather than of a cohesive nature. However, some other researches have shown that the strength of HBS is mainly influenced by methane hydrate (MH) in terms of cohesion because it bonds soil grains together [40,48] as shown in Fig. 1c, which has not been examined by Brugada et al. [2] yet. This constitutes one strong motivation of this study.

The distinct element method (DEM), which was proposed originally for dry granulates [3] and which treats soils as an assembly of discrete elements [3,18,24], has been more and more used in geotechnical engineering to investigate the macroscopic and microscopic responses of soils under different loading conditions [11,12,16,22,25,44,55], to examine the macroscopic constitutive models of granulates [12,13,49,50], to simulate the fracture process/macroscopic behavior of cohesive granular materials [4,6,7], to understand the penetration mechanism in granular ground [26] or in collapsing quicksand [32,33], and to obtain the landslide mechanism in very-rapid and extremely-rapid landslide process [19] or the evolution of natural cliffs subject to weathering [51]. Geo-researchers have also paid attention to cementation, since it is found that the mechanical behavior of natural sands is evidently distinct from that of the clean sands due to the existence of cementation between soil grains in them. In order to characterize this bonding behavior with DEM, Jiang et al. [17,27] have proposed a simple bond contact model for naturally microstructured sands. These studies show that the DEM incorporating with this simple model was able to capture the main features of naturally microstructured sands efficiently. Hence, in order to investigate the effect of MH cementation in Fig. 1c, a MH bond contact model should be established in a way similar to this simple model by experimental investigation first. However, since MH exists only under the condition of the very high pressure and low temperature, it is extremely difficult to carry out such a study on MH bonds directly in geo-laboratories. An alternative way is to carry out the experimental investigation on analogues, of which the relationships can be further extended to describe the microscopic behavior of bonded particles due to MH. Delenne et al. [5] first designed some experimental devices, and then characterized the behavior of bonds by performing simple loading tests on a pair of aluminum rods glued together by means of an epoxy resin. This work is quite convincing and impressive. However, it neglects the influence of normal force between grains on the bonding behavior probably due to technological difficulties. This unsatisfactory aspect constitutes another motivation of this study.

The main objective of the paper is to develop a simple distinct element modeling of the mechanical behavior of HBS with the MH distribution of cementation. First, to characterize the behavior of cohesive bond between particles under different normal forces, a set of mechanical tests on two bonded aluminum rods under different loading paths are performed with a specially designed apparatus. Then, the drained biaxial compression tests on DEM samples with different bond strengths, which are used to represent the HBS samples with different methane hydrate saturations (S_{MH}), are numerically carried out by our two-dimensional DEM code, NS2D [15,16,18,29] under different confining stresses. The code incorporates the simple bond

contact model obtained from the experimental data. Finally, the DEM results are compared with the experimental data acquired from triaxial compression tests on HBS samples performed previously by Miyazaki et al. [10] to demonstrate the capability of the method.

2 Experimental studies on cementation between particles

In this study, to characterize the bond behavior between soil grains under different normal forces experimentally, a set of bonded grains was idealized as a pair of aluminum rods glued together with an epoxy resin. Such a choice comes from two reasons: (1) As our first step in numerical analyses, two-dimensional DEM will be used, which needs the results obtained from experimental investigation on rods instead of spheres. (2) It is much more difficult to carry out experimental investigations on spheres than on rods in terms of sample preparation, loading devices etc. However, it is one of our future works to carry out experimental investigations on spheres. Figure 2 presents a schematic diagram of a pair of cemented aluminum rods. The rods are both 50 mm long with a diameter of 12 mm. This choice for the large ratio of length to diameter, about 4, is in order to simplify a three-dimensional problem as a plane strain problem during loading. As shown in Fig. 2, the cementation between the aluminum rods is 50 mm long and 3 mm wide. And its thickness along the line between the centers of the two rods is 0 mm. Note that such a pair of the bonded aluminum rods doesn't necessarily represent a real one in natural or artificially-made HBS, but makes it possible to carry out the tests on them in geo-laboratories. Therefore, a qualitative analysis of the bonding behavior can be obtained in this paper rather than a quantitative one.

To prepare many pairs of cemented rods in high quality repeatedly, a sample preparation device, which consists of the top and bottom parts, was specially designed as shown in Fig. 3. The procedure for preparing the samples with the device is as follows. First, a pair of aluminum rods were

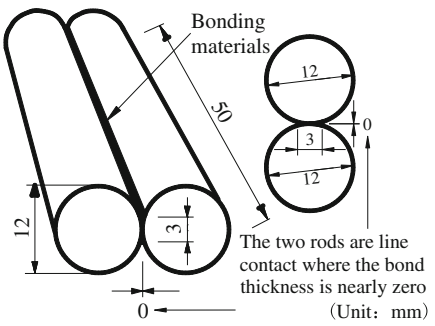

Fig. 2 Schematic diagram of idealized cemented rods in the experimental study

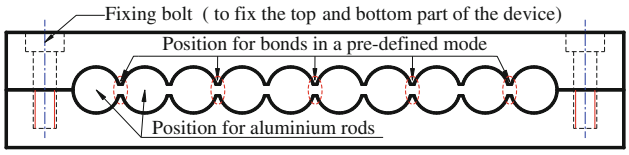

Fig. 3 Schematic diagram of the specimen preparation device

attached to each other after the epoxy resin was coated uniformly on the narrow and long surface of each rod with a spatula. The same way was repeated to prepare other four pairs of rods. Second, these five pairs of cemented rods were placed into the grooves of the bottom part of the device in order. Then, the top and bottom parts of the device were assembled together by fixing the bolts slowly. In this step, the overflowing epoxy resin squeezed out by the pressure must be wiped up. Finally, the five pairs of cemented rods together with the sample preparation device were kept in an air-conditioned room with a temperature of 20 °C for 24 h. After the bond strength is strong enough to form the samples, they were taken out of the device carefully and kept in a seal box for 28 days at 20 °C to make the epoxy resin achieve its target strength which would be examined later. This procedure is proved to be efficient in preparing high-equality samples.

In order to apply vertical (normal), horizontal (shear) forces and moments on the cemented rods independently, a set of auxiliary loading devices were specially designed, as illustrated in Fig. 4. These devices were used to carry out all the simple and complex loading tests, i.e. tension/compression tests, shearing/torsion tests under different normal forces, and shearing-torsion tests under different normal forces (155 tests in total). For all the tests, a deformation rate of 0.1 mm/min was used to apply vertical (normal) loads in tension/compression tests, and horizontal (shear) loads in other tests with the strain-controlled system. In this paper, since we only study the mechanical properties of HBS with a simple bond contact model which neglects the rolling resistance of cementation, the results of shearing-torsion tests under different normal forces are omitted for conciseness. The other test results will be described in detail in the following paragraphs.

Figure 5 provides the tensile force-displacement relationship of the cemented rods measured in the tension test. It shows that the tensile force increases almost linearly with the tensile displacement until the epoxy resin reaches its peak value and then it abruptly drops to zero, which can be characterized as an elastic-brittle-failure response. The measured tensile stiffness k_t and peak tensile strength R_t are about 8.0×10^7 N/m and 2.1 kN, respectively. The compressive force-displacement relationship of the cementation measured in the compression tests is provided in Fig. 6. It is found that the compressive force-displacement relationship is quite smooth and linear in the initial part before the epoxy

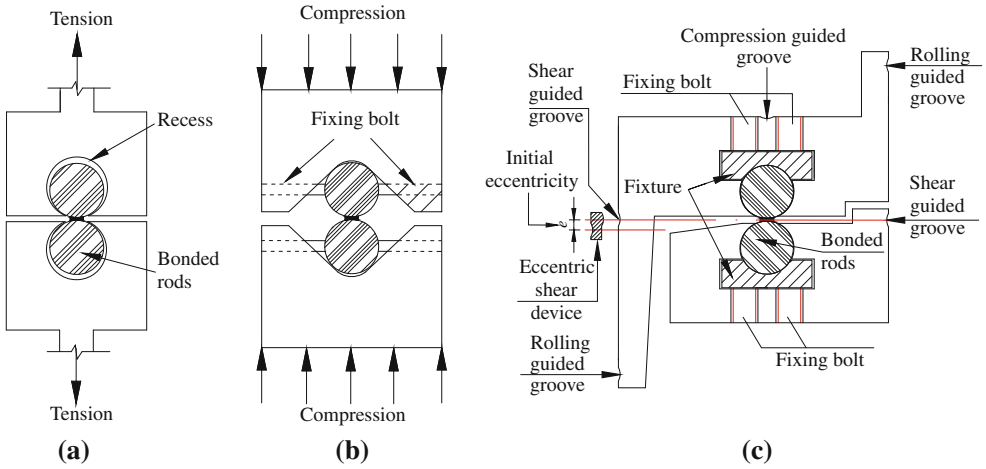

Fig. 4 Auxiliary test devices for mechanical examination on bonded rods: **a** tension device; **b** compression device; **c** complex stress device

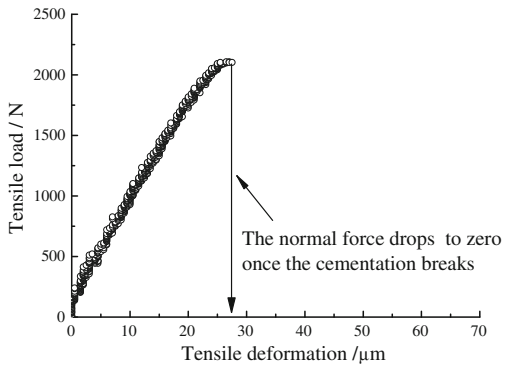

Fig. 5 Experimental data obtained from tension test on bonded aluminum rods

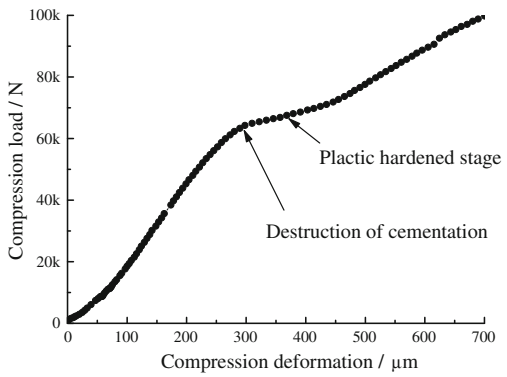

Fig. 6 The measured relationship by compression test on bonded aluminum rods

resin is crushed, which can be approximated by a linear elastic behavior. The measured compressive stiffness k_c and peak compressive strength R_c are about 2.1×10^8 N/m and 64 kN, respectively. After the epoxy resin is crushed, the compressive stiffness decreases significantly. However, as the epoxy resin is subsequently squeezed out, the compressive stiffness increases up to a constant value again finally due to the increasing of contact area between the two rods. Figure 7 presents the shearing force-displacement relationships obtained from shear tests on the cemented rods under different values of the normal force, i.e. $F_n = 0, 2, 4, 6, 8$ kN, respectively. As shown in Fig. 7, the shear force increases straightly with the shear displacement before the peak shear strength is achieved no matter what the value of the normal force is. Hence, it is fairly reasonable to assume a linear relationship between the shear force and displacement in this part. After the peak shear strength is achieved, the shear force abruptly drops to zero when the normal force F_n is zero, while it decreases to the residual shear strength linearly after the cementation experiences a strain softening stage when F_n is larger than zero. However, since the strain softening stage is quite short in the latter case, the relationship between the shear force and displacement in this part can be characterized with elastic-brittle-plastic performance, which will avoid the algorithmic complication in DEM analyses. Moreover, Fig. 7 shows that as the normal force increases, the initial shear stiffnesses k_s measured in the shear tests are almost the same, which is about 6.0×10^7 N/m. Figure 8 presents the relationships of the peak and residual shear strength against the normal force measured experimentally. Figure 8 shows that both the peak and residual shear strengths increase as the normal force increases, with the former in a slightly nonlinear way and the later in a nearly linear way.

3 DEM simulation of tests on HBS samples

3.1 A bond contact model for DEM analyses

In order to capture the bonding effect in naturally microstructured sands, Jiang et al. [17,27] proposed a simple bond contact model for discrete element modeling. The physical

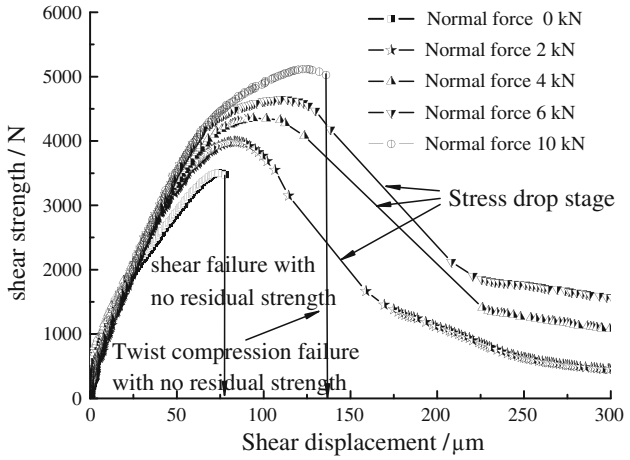

Fig. 7 The experimental data measured in shear test on bonded aluminum rods under different normal forces

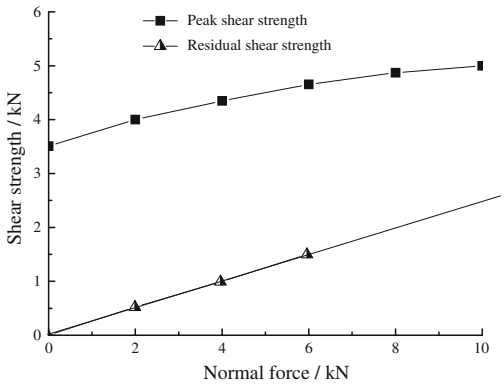

Fig. 8 Peak and residual shear strength of bonded aluminum rods under different normal forces

model is presented in Fig. 9 for the readability of the paper. In the subsection, we will improve it based on the experimental results introduced in the foregoing paragraphs, and then implement the improved one into our two-dimensional DEM code, NS2D, to simulate the biaxial compression tests on HBS samples.

To utilize the experimental results for modeling the bond behavior of cemented grains and obtain a simple bond contact model in DEM analyses, the main assumptions are as follows:

(1) The tensile force-displacement relationship of the cemented granules is simplified to be elastic-brittle-failure, of which the tensile stiffness is k_t. The cemented granules are detached and the tensile force drops to zero if the value of tensile force exceeds the tensile strength R_{tb}.
(2) The linear elastic property is employed to approximate the compressive mechanical behavior of the cemented granules, of which the compression stiffness is k_c.

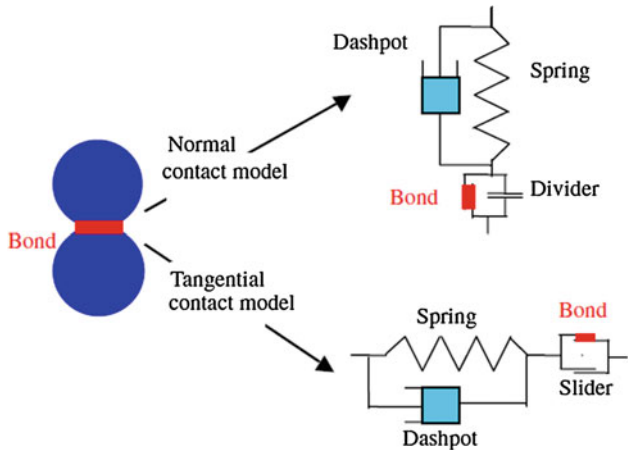

Fig. 9 Simple contact model proposed for bonds in the DEM analyses [18]

(3) The shear mechanical behavior of the cemented granules under the normal force is characterized to be elastic-brittle plastic, of which the shear stiffness is k_s. When the shearing force reaches the peak shear strength R_{sb}, it abruptly drops to the residual shear strength R_{sbr}, which is determined by the Mohr-Coulomb strength criterion.

Based on the above assumptions, a simple bond contact model can be obtained to describe the bond contact mechanical behavior of cemented granules, and is illustrated in Fig. 10, which neglects the mechanical response in the rolling direction [18,24,25]. In addition, the model does not incorporate the change in normal stiffness under a compressive loading, because (a) the change is quite slight as demonstrated in Fig. 6; (b) the deformation of soils, including granulates cemented whether by MH or other chemical materials, comes mostly from interparticle sliding and particle re-arrangement, instead of deformation at contacts [23,56,57]. This feature can be efficiently captured in the DEM model in which a constant stiffness is employed in both normal and tangential models [23,28,30]; (c) The use of a nonlinear stiffness will make DEM computation cost much more CPU time, but lead to little difference on the mechanical behavior of soils, than a linear stiffness.

Taking into account the effect of normal force F_n on the shear strength, we shall put forward a set of formula to determine the peak and residual shear strengths under different values of the normal force as follows:

$$\begin{cases} R_{sb} = R_{sbr} = 0 & (F_n \le -R_{tb}) \\ R_{sb} = R_{s0};\ R_{sbr} = 0 & (-R_{tb} < F_n \le 0) \\ R_{sb} = R_{s0} \cdot (1 + m \cdot F_n / R_{tb})^n \\ R_{sbr} = \mu \cdot F_n \end{cases} (0 < F_n \le R_{cb}) \\ R_{sb} = R_{sbr} = \mu \cdot F_n & (R_{cb} < F_n) \end{cases} \quad (1)$$

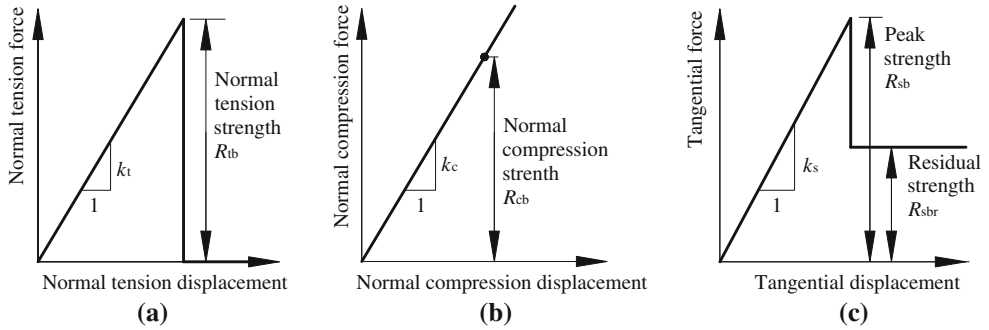

Fig. 10 Mechanical performance of the simple contact model of bonded rods: **a** normal tension contact model; **b** normal compression contact model; **c** tangential contact model

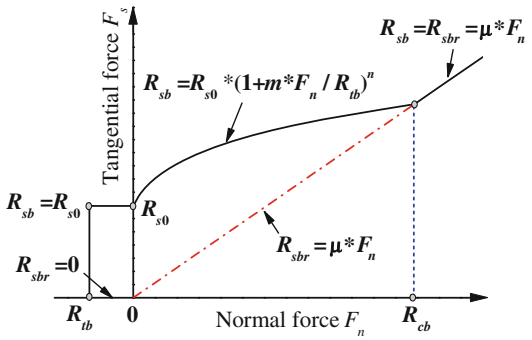

Fig. 11 The improved strength envelope of bonded rods used in DEM analysis

where R_{s0} is the peak shear strength at $F_n = 0$, R_{tb} the tensile strength, R_{cb} the compression strength, μ the inter-grain friction coefficient. m and n are two fitting parameters. In this paper, the values of these six parameters obtained from the experiment are 3.5, 2.1, 64 kN, 0.2, 1.0 and 0.216, respectively.

In comparison with the two previous studies [5,27,52], the main improved aspect lies in the relationships of the peak and residual shear strengths with the normal force, which are plotted in Fig. 11. As illustrated in Fig. 11, when $F_n \leq -R_{tb}$, the shear strength is zero due to the tensile destruction of cementation. When $-R_{tb} < F_n \leq 0$, due to the lack of the experimental data, it is assumed that when the bond is intact, the peak shear strength is equal to R_{s0}, i.e. the peak shear strength at $F_n = 0$, and the residual shear strength is zero once the bond is broken. This simplification will make the numerical computation much efficient with current PCs. When $0 < F_n \leq R_{cb}$, the peak shear strength increases non-linearly with the increasing of the normal force, and it finally equals to the residual shear strength at $F_n = R_{cb}$, while the residual shear strength increases linearly with the normal force which follows the Mohr-Coulomb strength criterion. When $F_n \leq R_{cb}$, due to the compressive crushing of the cementation, the peak and residual shear strength are equal to each other, both of which are determined by the Mohr-Coulomb strength criterion. Note that this local model has several advantages over Delenne' work [5], and in fact consists of three components, i.e. the models in normal, tangential and rolling directions [20,21]. However, we only used two components for the study, i.e. the models in normal and tangential directions, since an assembly of such contact models can be rigorously linked in theory with classical continuum mechanics [31].

In addition, there are several differences between our bond contact model, and the BPM model for rocks proposed by Potyondy and Cundall [45] and the bond contact models for snow [37,53]:

(a) The origin. By simplifying a pair of bonded particles as a macroscopic girder, the girder theory is used to derive the normal stress and shear stress in the bond to obtain the BPM model. This method does not take into account the local effects caused by particles on both the stress distribution within the bond and mechanical behavior of the bond, which violates the Saint-Venant principle. The cohesive particles interact with each other via the van der Waals forces in the first bond model for snow used by Vedachalam [53], while in the second bond model used by Vedachalam [53] (i.e. the JKR model), the cohesive force comes from the surface energy, which acts in combination with Hertz elastic model. The third bond model for snow used by Favier et al. [37] is composed of a linear hysteretic cohesive model in normal direction proposed by Luding [38,39] and a capillary-water like cohesive model in tangential direction proposed by Jiang et al. [16]. In comparison, the bond contact model comes from the experimental observation, in which different types of forces are directly applied to pairs of bonded particles to obtain the mechanical behavior of bonded contact.

(b) The failure criteria. In the BPM model, the peak shear force keeps constant firstly, and then increases linearly with the increasing of normal force; the peak torque (i.e. the peak bond rolling resistance) increases linearly with the increasing of normal forces. In addition, the shear force-torque strength envelope is in rectangular shape. In all the three bond models

for snow, the peak shear force increases linearly with the increasing of normal force, while bond rolling resistance is neglected. In comparison, in our complete bond model [20,21], both the peak shear force and the peak rolling resistance increase parabolically at first, and then increase linearly with the increasing of normal force. The peak shear force-peak rolling resistance strength envelope is in an elliptical shape. Note again that that bond rolling resistance is not taken into account in the simplified bond contact model in this article.

For simplicity and based on experimental observation, R_{s0} can be further assumed to be 1.66 R_{tb}. In the light of fact that the inter-grain friction coefficient μ is usually different from that between aluminum rods, Eq. (1) can be further expressed for the DEM analyses as

$$\begin{aligned}
&R_{sb} = R_{sbr} = 0 && (F_n \le -R_{tb})\\
&R_{sb} = 1.66R_{tb};\ \ R_{sbr} = 0 && (-R_{tb} < F_n \le 0)\\
&R_{sb} = 1.66R_{tb} \cdot (1 + F_n/R_{tb})^{0.216}\\
&R_{sbr} = \mu \cdot F_n && (0 < F_n \le R_{cb})\\
&R_{sb} = R_{sbr} = \mu \cdot F_n && (R_{cb} < F_n)
\end{aligned} \tag{2}$$

in which R_{tb} can be regarded as a parameter solely controlling the size of strength envelope of bonds, and hence will be used to represent methane hydrate saturation (S_{MH}) in the DEM analyses in this paper. It is true that MH bonds can be created by following a kinetic law, and may damage due to aging effects. Such time effects are indeed the formation/dissolution process of MH bonds, which depends on the pressure and temperature in the environment. It is one of our future works to relate this model to the real behavior of MH bonds, microscopically and quantitatively, in the light of the pressure and temperature in the environment.

3.2 Preparation of DEM samples

The above model was implemented in a two-dimensional distinct element method (DEM) code, NS2D [16,18,29], which was used in this investigation. Each of the two-dimensional DEM samples was rectangle in shape with a width of 400 mm and a height of 700 mm. And it was composed of 10 kinds of discs with different diameters, 5,000 discs in total. Fig. 12 presents the grain size distribution of all the samples used in this study. The DEM material was of a maximum diameter of 9.0 mm, a minimum diameter of 6.0 mm, an average grain diameter $d_{50} = 7.6$ mm and an uniformity coefficient $C_u = d_{60}/d_{10} = 1.3$. The particle density was 2.65 g/cm^3 and the planar void ratio of the specimen at initial state was set to be 0.28.

The DEM specimens with the target properties described above were prepared in three steps:

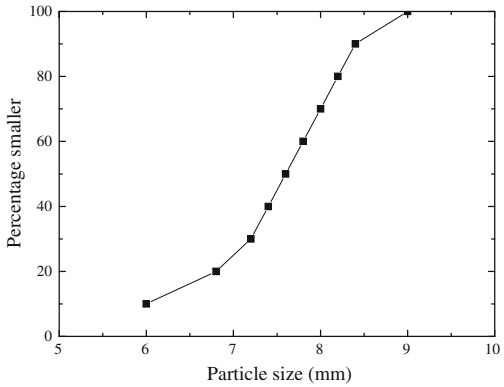

Fig. 12 Grain size distribution of material used in the DEM numerical simulation

Table 1 The contact stiffness and bond strength used for DEM simulation in this paper

Loading path	Stiffness (N/m)	Bond strength (kN)
Tension	1.5×10^8	0, 1.0, 2.0
Compression	1.5×10^8	No failure
Shear	1.0×10^8	Equation (2)

(1) Prepare loose uncemented specimens with the specific planar void ratio, i.e. 0.28 in the investigation, by means of the multi-layer under-compaction method (UCM) [15].
(2) Compress the specimens in one-dimensional direction with a vertical pressure of 12.5 kPa while the horizontal boundaries are fixed until the specimens arrive at their equilibrium states.
(3) Form cementation at each contact point in specimens, of which the mechanical behavior is governed by the bond contact model proposed in the previous paragraphs. Three different values of bond strength, i.e. R_{tb} = 0, 1.0 and 2.0 kN respectively, are adopted in the DEM numerical simulations to represent the different hydrate saturations of HBS in the paper.

The values of the contact stiffness and bond strength used in the DEM numerical simulations are listed in Table 1. In addition, the friction coefficient between particles μ is 0.5 and that between particle and wall is zero. Note that the same bond strength was assigned to all the contacts in each kind of DEM samples. In fact, however, the bond strength caused by methane hydrate in HBS is hardly the same at different contacts due to the spacious variation in natural environment. This assumption may lead to some discrepancies in mechanical behavior with natural HBS, but will not influence the main conclusions in this paper and it will be one of our future works.

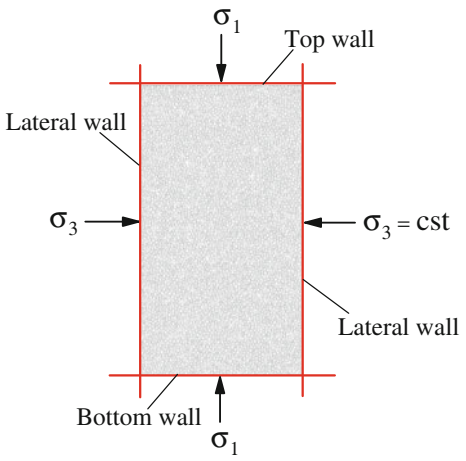

Fig. 13 Procedure for DEM biaxial compression tests

3.3 DEM simulation of the biaxial compression tests on HBS samples

A series of drained biaxial compression tests were carried out on the loose DEM specimens with initial planar void ratio 0.28 and bond strength $R_{\mathrm{tb}} = 0, 1.0, 2.0$ kN, respectively, under different confining stresses σ_3. This is a conventional test used in Geomechanics and Geotechnical Engineering to examine the mechanical behaviour of soils, which procedure will be introduced with the help of Fig. 13. First, the specimens were consolidated under the confining stress σ_3 of 50, 100, and 200 kPa, respectively. Then, they were compressed vertically by moving the top and bottom walls downwards and upwards respectively, at the given rate of 0.1 %/min, while the positions of lateral walls were adjusted by a numerical servo-technique to guarantee that the confining stress, i.e. $\sigma_3 = 50, 100$, and 200 kPa respectively, always remained constant. Such a low strain rate is necessary to guarantee the quasi-static deformation of the specimens and the homogenous stress field before the possible emergence of strain localization in specimens. In the numerical simulations, all the wall boundaries were rigid and always frictionless.

In addition, the vertical stress is noted as σ_1, horizontal stress (i.e. confining stress) σ_3, mean stress $p = (\sigma_1 + \sigma_3)/2$, and deviatoric stress $q = (\sigma_1 - \sigma_3)/2$ to describe the numerical results in the next section.

4 Comparison between numerical and experimental results of HBS samples

4.1 Stress-strain behavior

Figure 14 presents the deviatoric stress-axial strain relationships of DEM HBS samples with different bond strengths under different confining stresses. Figure 14 shows that:

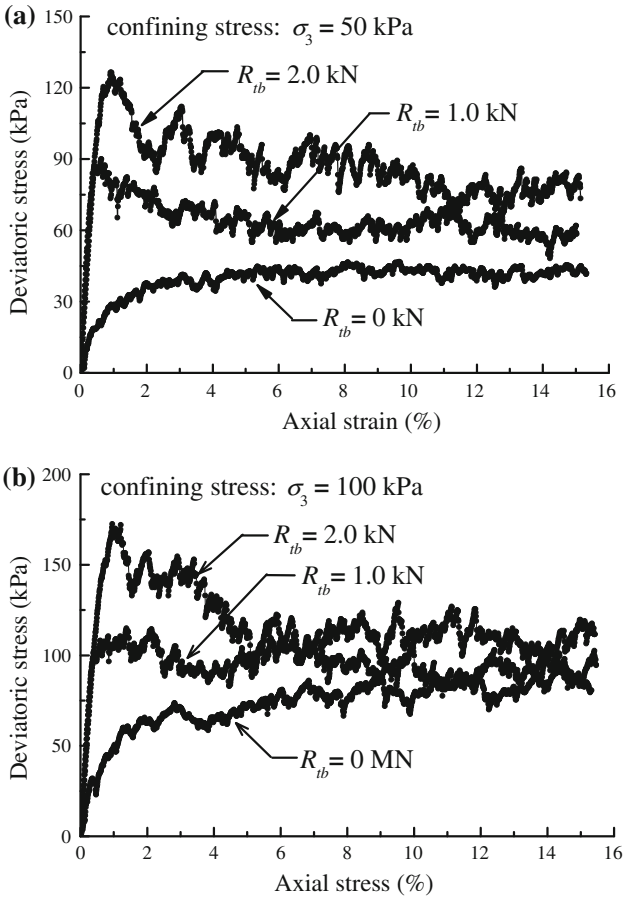

Fig. 14 Stress–strain relationships of the DEM samples with different bond strength R_{tb} under different confining stresses σ_3: **a** $\sigma_3 = 50$ kPa; **b** $\sigma_3 = 100$ kPa

(1) When there is no cementation between soil particles, the stress-strain behavior of DEM HBS samples exhibits strain hardening characteristic, while its stress-strain behavior exhibits strain softening characteristic when the cementation is formed in DEM HBS samples. In addition, the strain softening characteristic is more and more significant with the increasing of the bond strength.
(2) Bond strength has a significant influence on the peak shear strengths of DEM HBS samples. And the peak shear strength increases as bond strength increases.
(3) Comparing Fig. 14a with b, it is found that the peak shear strengths of DEM HBS samples increase significantly with the increasing of the confining stress.
(4) The residual shear strengths of all DEM HBS samples with different bond strengths approximate to the peak shear strength of DEM HBS samples which have no cementation between soil particles.

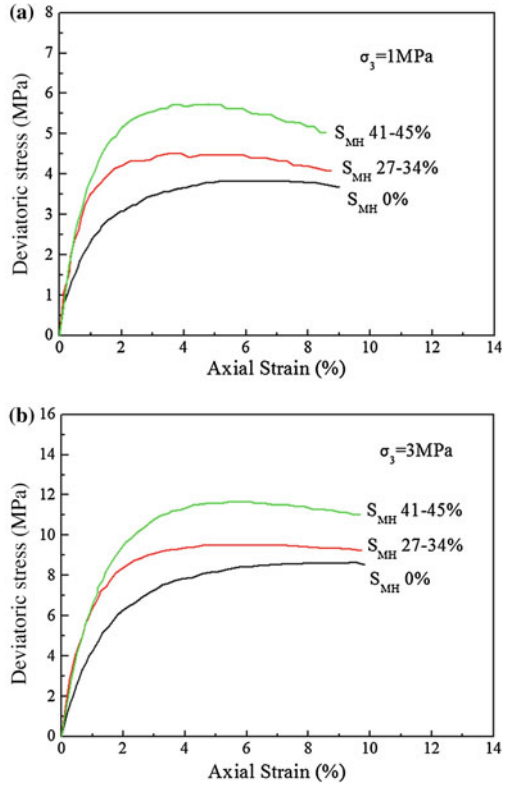

Fig. 15 Stress–strain results from drained triaxial tests on synthetic methane hydrate sediments with different hydrate saturation under different confining stresses σ_3: **a** $\sigma_3 = 1$ MPa; **b** $\sigma_3 = 3$ MkPa. The *graph* is redrawn from Miyazaki et al. [10]

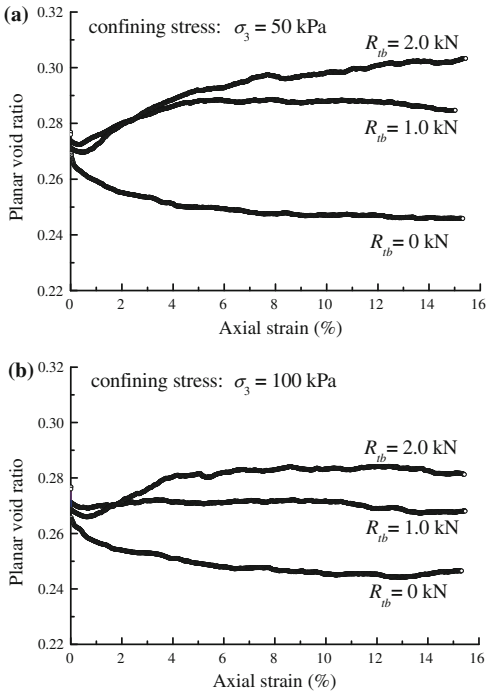

Fig. 16 Volumetric-axial strain relationships of the DEM samples with different bond strengths R_{tb} under different confining stress σ_3: **a** $\sigma_3 = 50$ kPa; **b** $\sigma_3 = 100$ kPa

Figure 15 provides the results of drained triaxial compression tests on the real HBS samples with different S_{MH} carried out by Miyazaki et al. [10]. It is found that the stress-strain behavior of HBS samples changes from strain hardening characteristic to strain softening characteristic as S_{MH} increases and the strain softening characteristic is more and more significant as increasing of S_{MH}. In addition, the peak shear strength increases as S_{MH} increases. By comparing Fig. 14 with 15, it can be included that the DEM results are qualitatively in agreement with the experimental results in terms of the variation trend of the dilation and the peak shear strength.

4.2 Volumetric response during biaxial compression test

Figure 16 provides the relationships between the volumetric and axial strain of HBS with different bond strengths under different confining stresses. Note that the positive volumetric strain denotes dilation in this figure. As shown in Fig. 16, the volumetric change characteristic of the unbonded sands is always shear contraction, while the DEM HBS samples which have cementation between soil particles show significant dilation after an initial shear contraction. In addition, the dilation increases as the bond strength increases and decreases as the confining stress increases.

Figure 17 provides the experimental result obtained by Miyazaki et al. [10]. As shown in Fig. 17, the real HBS sample exhibits significant dilation, which increases with the increasing of S_{MH} but decreases with confining stress. Such a feature is also in agreement with the simulation results as shown in Fig. 16. Hence, the method incorporating the proposed bond contact model in this paper can qualitatively reflect the relationship between the volumetric and axial strain of real HBS.

4.3 Peak shear strength of HBS samples

Figure 18 provides the peak shear strength envelope, the cohesion and the friction angle of DEM HBS samples with different bond strengths. As shown in Fig. 18, both the cohesion and friction angle increase as bond strength increases. Whereas, the influences of bond strength on them are different: the influence on the cohesion is much more significant than on the friction angle. This conclusion is in accordance with the result reported by Soga et al. [48].

Figure 19 presents the experimental results obtained by Miyazaki et al. [10]. As shown in Fig. 19, the cohesions of real HBS samples increase significantly with the increasing of S_{MH}, while the friction angles are almost invariable as S_{MH} increases. By comparing Fig. 18 with 19, it is found that the

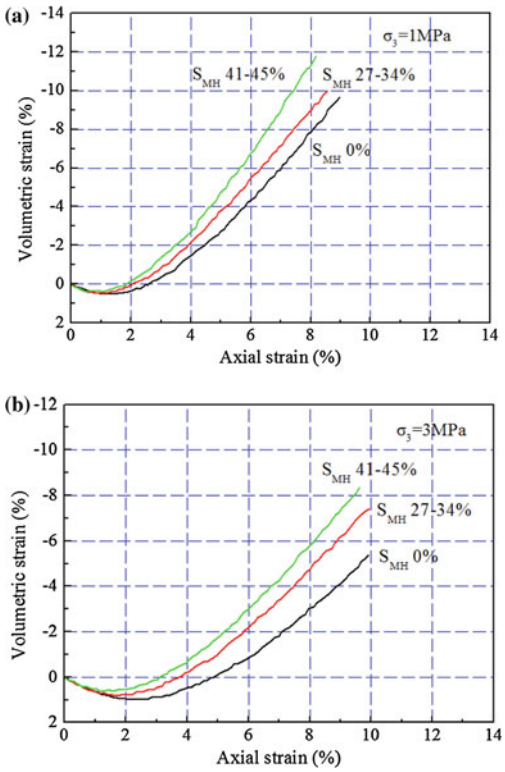

Fig. 17 Volumetric-axial strain result from drained triaxial tests on synthetic methane hydrate sediments with one hydrate saturation under different confining stresses σ_3: **a** $\sigma_3 = 1$ MPa; **b** $\sigma_3 = 3$ MkPa. The *graph* is redrawn from Miyazaki et al. [10]

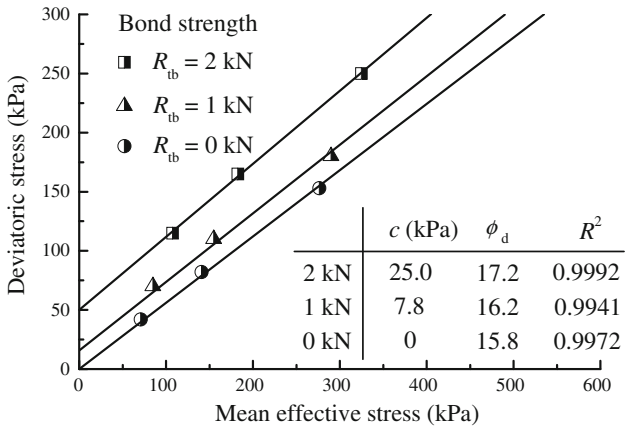

Fig. 18 Peak strength envelops of the DEM samples with different bond strengths R_{tb}

DEM simulation in this paper can capture the strength feature of real HBS samples efficiently and essentially.

5 Discussion on main limitations

The purpose of this investigation is to develop a simple distinct element modeling of the mechanical behavior of HBS,

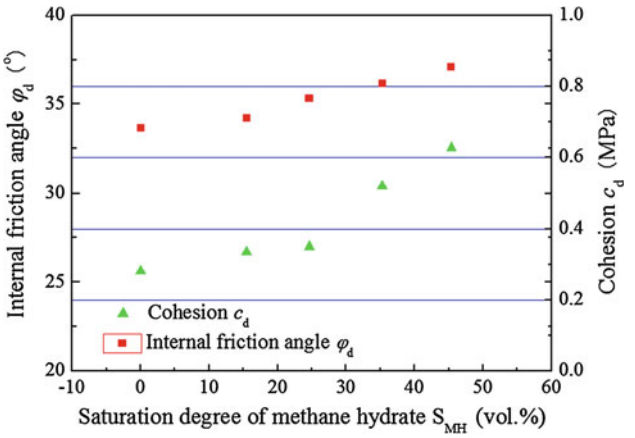

Fig. 19 Internal friction angle ϕ_d and cohesion c_d versus saturation degree of methane hydrate S_{MH}. The graph is redrawn from Miyazaki et al. [10]

in which the hydrate acts as cementation between soil grains, which will provide a basis for the future study on the mechanical behavior of HBS and its macroscopic constitutive models. Although the obtained DEM results are generally in agreement with the experimental observation, the following limitations need to be overcome in future.

(1) Only the influence of one hydrate distribution in HBS, i.e. cementation, on the mechanical behavior of HBS samples was captured and investigated, while the influences of other distributions which may be important in controlling the mechanical behavior of HBS were ignored in this paper.
(2) Since a 2-D DEM code was developed, the planar samples were used to study the mechanical behaviour of HBS instead of the three-dimensional cylindrical samples. This difference may lead to some discrepancies in the physical or mechanical behavior due to the different initial properties of these two kinds of samples, for example, the void ratio.
(3) Different values of bond strength were employed to represent different hydrate saturations, i.e. the large value of bond strength corresponding to large S_{MH}. It should be noted that the exact relationship between the bond strength and S_{MH} has been unknown yet and needs to be clarified, although the qualitative relationship, i.e. the bond strength increases with the increasing of S_{MH}, stands.

6 Conclusions

This paper presented a simple distinct element modeling of the mechanical behavior of hydrate-bearing sediments (HBS) in deep seabed. Well glued aluminum rods were

loaded under various loading paths to obtain the mechanical behavior of cemented particles. Based on the laboratory tests, an improved bond contact model was proposed to describe the bond behavior between particles in HBS, and then implemented into a two-dimensional DEM code, NS2D, for numerical simulations. A series of drained biaxial compression tests were numerically carried out to study the mechanical behavior of HBS. Finally, the simulation results were compared with the experimental results obtained by Miyazaki et al. [10]. The following conclusions can be made from the investigation:

(1) The experimental investigation on idealized bonded particles highlights the microscopic mechanical response of the cemented soil particles. The cemented particles fails abruptly under the simple loading path, while ductile failure is observed under combined loading paths. Approximate linear elasticity dominates the pre-failure stage of the mechanical behavior under all loading paths, although a global non-linearity is often observed. Furthermore, the inter-particle shear strength depends on the normal force applied on the particles, which can be calculated with the proposed formula when the bond is intact and with the Mohr-Coulomb strength criterion when the bond fails.
(2) Compared with the experimental results, the DEM numerical results demonstrate that the proposed method incorporating the new bond contact model can capture the following main features of the mechanical behavior of HBS efficiently: (a) the strain softening characteristic is more and more significant with the increasing of S_{MH}; (b) the peak shear strength increases as S_{MH} or the confining stress increases; (c) the dilation increases as S_{MH} increases or the confining stress decreases; (d) both the cohesion and friction angle increase with the increasing of S_{MH}, but the influence of S_{MH} on the cohesion is much more significant than on the friction angle.

Note that one of the main aims is to establish a simple model for MH soils, in which different bond strengths are used to represent different methane hydrate saturations (S_{MH}). It is one of our future works to relate this model to the real behavior of MH bonds, microscopically and quantitatively, in the light of the pressure and temperature in the environment, and take into account a kinetic law describing the formation/dissolution process of MH bonds, which can be implemented into DEM codes to simulate both element tests [6,10,14,17,40–42] and boundary-value problems [8,23,26,29,32–35,43].

Acknowledgments This work was funded by China National Funds for Distinguished Young Scientists with Grant No. 51025932, and PhD Programs Foundation of Ministry of Education of China with Grant No. 20100072110048.

References

1. Brown, H.E., Holbrook, W.S., Hornbach, M.J., Nealon, J.: Slide structure and role of gas hydrate at the northern boundary of the Storegga Slide, offshore Norway. Marine Geol. **229**(3–4), 179–186 (2006)
2. Brugada, J., Cheng, Y.P., Soga, K., Santamarina, J.C.: Discrete element modelling of geomechanical behaviour of methane hydrate soils with pore-filling hydrate distribution. Granul Matter **12**, 517–525 (2010)
3. Cundall, P.A., Strack, O.D.L.: The discrete numerical model for granular assemblies. Géotechnique **29**(1), 47–65 (1979)
4. D'Addetta, G.A., Kun, F., Ramm, E.: On the application of a discrete model to the fracture process of cohesive granular materials. Granul. Matter **4**(2), 77–90 (2002)
5. Delenne, J.Y., Youssoufi, M.S.E., Cherblanc, F., Bénet, J.C.: Mechanical behaviour and failure of cohesive granular materials. Int. J. Numer. Anal. Met. **28**(15), 1577–1594 (2004)
6. Estrada, N., Lizcano, A., Taboada, A.: Simulation of cemented granular materials: I. Macroscopic stress-strain response and strain localization. Phys. Rev. E **82**, 011303 (2010)
7. Estrada, N., Lizcano, A., Taboada, A.: Simulation of cemented granular materials: II. Micromechanical description and strength mobilization at the onset of macroscopic yielding. Phys. Rev. **E82**, 011304 (2010)
8. Freij-Ayoub, R., Tan, C., Clennell, B., Tohidi, B., Yang, J.H.: A wellbore stability model for hydrate bearing sediments. J. Petrol. Sci. Eng. **57**, 209–220 (2007)
9. Grozic, J.L.H., Ghiassian, H.: Undrained shear strength of methane hydrate-bearing sand: Preliminary laboratory results. In: Proceedings 6th Canadian Permafrost Conference and 63rd Canadian Geotechnical Conference, Calgary, pp. 459–466 (2010)
10. Miyazaki, K., Masui, A., Sakamoto, Y., Aoki, K., Tenma, N., Yamaguchi, T.: Triaxial compressive properties of artificial methane-hydrate-bearing sediment. J. Geophys. Res. **116**, B06102 (2011)
11. Iwashita, K., Oda, M.: Rolling resistance at contacts in simulation of shear band development by DEM. J. Eng. Mech. **124**(3), 285–292 (1998)
12. Jiang, M.J., Harris, D., Yu, H.S.: Kinematic models for non-coaxial granular materials: Part I: Theories. Int. J. Numer. Anal. Met. **29**(7), 643–661 (2005)
13. Jiang, M.J., Harris, D., Yu, H.S.: Kinematic models for non-coaxial granular materials: Part II: Evaluation. Int. J. Numer. Anal. Met. **29**(7), 663–689 (2005)
14. Jiang, M.J., Harris, D., Zhu, H.H.: Future continuum models for granular materials in penetration analyses. Granul. Matters **9**, 97–108 (2007)
15. Jiang, M., Konrad, J.M., Leroueil, S.: An efficient technique for generating homogeneous specimens for DEM studies. Comput. Geotech. **30**, 579–597 (2003)
16. Jiang, M.J., Leroueil, S., Konrad, J.M.: Insight into strength functions in unsaturated granulate by DEM analysis. Comput. Geotech. **31**(6), 473–489 (2004)
17. Jiang, M.J., Leroueil, S., Konrad, J.M.: Yielding of microstructured geomaterial by distinct element method analysis. J. Eng. Mech. ASCE **131**(11), 1209–1213 (2005)
18. Jiang, M.J., Leroueil, S., Zhu, H.H., Yu, H.S., Konrad, J.M.: Two-Dimensional discrete element theory for rough particles. Int. J. Geomech. ASCE **9**(1), 20–33 (2009)
19. Jiang, M.J., Murakami, A.: Distinct element method analyses of idealized bonded-granulate cut slop. Granul. Matter **14**, 393–410 (2012)
20. Jiang, M.J., Sun, Y.G., Li, L.Q., Zhu, H.H.: Contact behavior of idealized granules bonded in two different interparticle distances: An experimental investigation. Mech. Mater. **55**, 1–15 (2012)

21. Jiang, M.J., Sun, Y.G., Xiao, Y.: An experimental investigation on the mechanical behavior between cemented granules. Geotech. Test. J. (ASTM) **35**(5), 678–690 (2012)
22. Jiang, M.J., Yan, H.B., Zhu, H.H., Utili, S.: Modeling shear behavior and strain localization in cemented sands by two-dimensional distinct element method analyses. Comput. Geotech. **38**, 14–29 (2011)
23. Jiang, M.J., Yin, Z.Y.: Analysis of stress redistribution in soil and earth pressure on tunnel lining using the discrete element method. Tunn. Undergr. Space Technol. **32**, 251–259 (2012)
24. Jiang, M.J., Yu, H.S., Harris, D.: A novel discrete model for granular material incorporating rolling resistance. Comput. Geotech. **32**(5), 340–357 (2005)
25. Jiang, M.J., Yu, H.S., Harris, D.: Bond rolling resistance and its effect on yielding of bonded granulates by DEM analyses. Int. J. Numer. Anal. Met. **30**(7), 723–761 (2006)
26. Jiang, M.J., Yu, H.S., Harris, D.: Discrete element modelling of deep penetration in granular soils. Int. J. Numer. Anal. Met. **30**(4), 335–361 (2006)
27. Jiang, M.J., Yu, H.S., Leroueil, S.: A simple and efficient approach to capturing bonding effect in naturally microstructured sands by discrete element method. Int. J. Numer. Methods Eng. **69**, 1158–1193 (2007)
28. Jiang, M.J., Zhang, W.C., Sun, Y.G., Utili, S.: An investigation on loose cemented granular materials via DEM analysis. Granul. Matter. (2013) doi:10.1007/s10035-012-0382-8 (online)
29. Jiang, M.J., Zhu, H.H., Harris, D.: Classical and non-classical kinematic fields of two-dimensional penetration tests on granular ground by discrete element method analyses. Granul. Matter **10**, 439–455 (2008)
30. Jiang, M.J., Zhu, H.H., Li, X.M.: Strain localization analyses of idealized sands in biaxial tests by distinct element method. Front. Architect. Civil Eng. China (FAC) **4**(2), 208–222 (2010)
31. Jiang, M.J., Zhu, H.H.: An interpretation of the internal length in Chang's couple-stress continuum for bonded granulates. Granul. Matter **9**, 431–437 (2007)
32. Kadau, D., Andrade Jr., J.S., Herrmann, H.J.: Collapsing granular suspensions. Eur. Phys. J. E **30**, 275–281 (2009)
33. Kadau, D., Andrade Jr., J.S., Herrmann, H.J.: A micromechanical model of collapsing quicksand. Granul. Matter **13**, 219–223 (2011)
34. Kayen, R.E., Lee, H.J.: Pleistocene slope instability of gas hydrate-laden sediment on the Beaufort Sea Margin. In: Proceedings 3rd Biot Conference on Poromechanics, vol. 10, pp. 125–141 (1991)
35. Klar, A., Soga, K., Ng, M.Y.A.: Coupled deformation-flow analysis for methane hydrate wells. Marine Geotechnology, Oklahoma, pp. 652–659 (2005)
36. Konno, Y., Oyama, H., Nagao, J., Masuda, Y., Kurihara, M.: Numerical analysis of the dissociation experiment of naturally occurring gas hydrate in sediment cores obtained at the Eastern Nankai Trough, Japan. Energy Fuels **24**, 6353–6358 (2010)
37. Favier, L., Daudon, D., Donzé, F.V.: Rigid obstacle impacted by a supercritical cohesive granular flow using a 3D discrete element model. Cold Reg. Sci. Technol. **85**, 232–241 (2013)
38. Luding, S.: Cohesive, frictional powders: Contact models for tension. Granul. Matter **10**, 235–246 (2008)
39. Luding, S., Manetsberger, K., Müllers, J.: A discrete model for long time sintering. J. Mech. Phys. Solids **53**, 455–491 (2005)
40. Masui, A., Haneda, H., Ogata, Y., Aoki, K.: Effects of methane hydrate formation on shear strength of synthetic methane hydrate sediments. In: Proceedings of the Fifteenth International Offshore and Polar Engineering Conference. June 19–24, Seoul, Korea (2005)
41. Masui, A., Haneda, H., Ogata, Y., Aoki, K.: The effect of saturation degree of methane hydrate on the shear strength of synthetic methane hydrate sediments. In: Proceedings of the 5th International Conference on Gas Hydrates. June 13–16, Trondheim, Norway. Paper No. 2037 (2005)
42. Miyazaki, K., Masui, A., Sakamoto, Y., Aoki, K., Tenma, N., Yamaguchi, T.: Triaxial compressive properties of artificial methane-hydrate-bearing sediment. J. Geophys. Res. **116**, B06102 (2011)
43. Nixon, M.F., Grozic, J.L.H.: Submarine slope failure due to hydrate dissociation: A preliminary quantification. Can. Geotech. J. **44**, 314–325 (2007)
44. Oda, M., Iwashita, K.: Study on pair stress and shear band development in granular media based on numerical simulation analyses. Int. J. Eng. Sci. **38**, 1713–1740 (2000)
45. Potyondy, D.O., Cundall, P.A.: A bonded-particle model for rock. Int. J. Rock Mech. Min. Sci. **41**, 1329–1364 (2004)
46. Rutqvist, J., Grover, T., Moridis, G.J.: Coupled hydrologic, thermal and geomechanical analysis of well bore stability in hydrate-bearing sediments. OTC 19572, Offshore Technology Conference. May 5–8, Houston, Texas, USA (2008)
47. Rutqvist, J., Moridis G., Grover, T., Collett, T.: Geomechanical response of known permafrost hydrate deposits to depressurization induced production. In: 6th International Conference on Gas Hydrates, Chevron, Vancouver, BC, Canada. Paper No. 5726 (2008)
48. Soga, K., Lee, S.L., Ng, M.Y.A., Klar, A.: Characterization and engineering properties of methane hydrate soils. In: Phoon, K.K., Hight, D.W., Leroueil, S., Tan, T.S. (eds.) Characterization and Engineering Properties of Natural Soils, vol. 4. Taylor and Francis, London, pp. 2591–2642 (2006)
49. Thornton, C.: Numerical simulations of deviatoric shear deformation of granular media. Géotechnique **50**(1), 43–53 (2000)
50. Thornton, C., Zhang, L.: Anumerical examination of shear banding and simple shear non-coaxial flow rules. Philos. Mag. **86**(21–22), 3425–3452 (2006)
51. Utili, S., Crosta, G.B.: Modelling the evolution of natural cliffs subject to weathering: 2. Discrete element approach. J. Geophys. Res. **116**, F01017 (2011)
52. Utili, S., Nova, R.: DEM analysis of bonded granular geomaterials. Int. J. Numer. Anal. Methods Geomech. **32**, 1997–2031 (2008)
53. Vedachalam, V.: Discrete Element Modelling Of Granular Snow Particles Using LIGGGHTS. Ph.D Dissertation. Edinburgh Parallel Computing Centre. The University of Edinburgh, UK. August (2011)
54. Waite, W.F., Santamarina, J.C., Cortes, D.D., Dugan, B., Espinoza, D.N., Germaine, J., Jang, J., Jung, J.W., Kneafsey, T.J., Shin, H., Soga, K., Winter, W.J., Yun, T.S.: Physical properties of hydrate-bearing sediments. Rev. Geophys. **47**, 1–38 (2009)
55. Wang, J., Jiang, M.J.: Unified soil behavior of interface shear test and direct shear test under the influence of lower moving boundaries. Granul. Matter **13**(5), 631–741 (2011)
56. Wang, Y.H., Leung, S.C.: A particular-scale investigation of cemented sand behavior. Can. Geotech. J. **45**(1), 29–44 (2008)
57. Wang, Y.H., Leung, S.C.: Characterization of cemented sand by experimental and numerical investigations. J. Geotech. Geoenviron. Eng. (ASCE) **134**(7), 992–1004 (2008)